

Recent Progress in Defective Carbon-Based Oxygen Electrode Materials for Rechargeable Zink-Air Batteries

Sidi Wang,^[a] Hongliang Jiang,*^[a] and Li Song^[a]

In recent years, rechargeable Zn-air batteries put forward higher requirements on oxygen electrode materials in terms of their bifunctional properties, stability, and economic cost. As an eligible candidate, defective carbon-based nanomaterials have attracted considerable attention since substantial progresses in oxygen evolution reaction and/or oxygen reduction reaction have been reported sequentially. This review briefly summarizes the recent advancements towards defective carbon-based oxy-

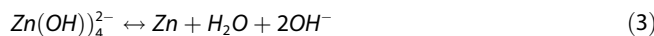
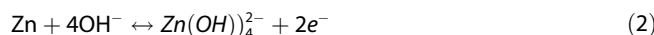
gen electrode materials, mainly focusing on the structure-designing strategies and characterization techniques of active centers, as well as the understanding of structure-property relationships by the combination of experimental result and theoretical calculation for rechargeable Zn-air batteries. Besides, the current challenges and opportunities in high-performance carbon electrodes are discussed with an emphasis on future probable solutions.

1. Introduction

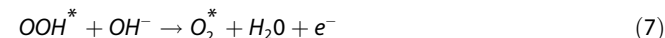
Recent years have witnessed the soaring achievements in electrochemical storage and conversion for environment and energy issues.^[1] In all the applications, rechargeable Zn-air batteries (ZABs) have become a spotlight recently due to their much higher energy density and lighter weight compared to lead and lithium-ion batteries. The theoretical specific energy density of the Zn-air cell is 1084 Wh kg^{-1} , which possesses obvious superiority relative to Li-ion batteries.^[2] The outstanding performance attributes to their special configuration where Zn or Zn composites are appropriate as the anodes while the cathodic active material, oxygen, is directly accessed from the atmosphere during discharge. The overall reaction pathway is:



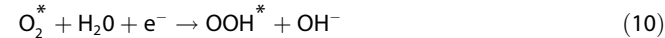
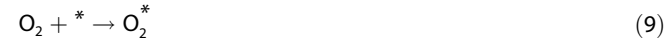
The Zn metal reacts at the anode in alkaline solution as follows:



The cathodic reactions of ZABs are oxygen reduction reaction (ORR) during discharging and oxygen evolution reaction (OER) during recharging, respectively. In the alkaline environment of ZABs, it is well accepted that the OER happens at charging process by following four-electron (4e^-) steps^[3]:



The relevant ORR mechanism is recognized as the reverse process of OER,^[4] as shown below:



where * represents the active state. OH*, OOH*, O* and O₂* are the reactive intermediates. The 4e⁻ pathway is considered as the optimum for oxygen electrocatalyst, but a 2×2e⁻ transfer way often occurs in ORR, leading to the production of H₂O₂ and subsequent decrease of catalytic efficiency.^[5] Therefore, achieving 4e⁻ dominant pathway is anticipated as the target for boosting oxygen catalysis.

In fact, the sluggish kinetics of both OER and ORR impedes the developments of rechargeable Zn-air batteries.^[6] Therefore, it is highly required to select the bifunctional oxygen electrode materials with superior catalytic performance. It is noteworthy that it is hard to directly relate the battery performance (such as open-circuit potential, charge/discharge profiles, capacity retention data, etc) with the intrinsic properties of electrode materials. Generally, efficient bifunctional oxygen electrocatalysis (ORR/OER) suggests good performance of the electrocatalysts in assembled rechargeable Zn-Air batteries. In this regard, the charge voltage, discharge voltage and the voltage gap between them can be used to evaluate the bifunctional performance of the electrocatalysts in the Zn–air battery. As

[a] S. Wang, Dr. H. Jiang, Prof. L. Song
National Synchrotron Radiation Laboratory
CAS Center for Excellence in Nanoscience
University of Science and Technology of China
Hefei, Anhui 230026, P. R. China.
E-mail: jhlworld@ustc.edu.cn

An invited contribution to a Special Collection dedicated to Metal-Air Batteries

we know, Pt/C and IrO₂ are considered as the benchmark materials for ORR and OER, respectively.^[7] However, some drawbacks of noble metal-based electrocatalysts like high cost and bad long-term durability block the commercialization. What's more, the monofunctionality could not meet the demand of reversible charging and discharging processes. Alternatively, carbon-based nanomaterials with various defects attract the interest of a number of researchers after Dai's pioneering NCNT work on ORR.^[8] A huge amount of advantages have been obtained, including the following aspects: 1) High conductivity. The unbound electrons dissociated in sp² carbon structure can guarantee the rapid charge transportation in redox reactions to enhance electrocatalytic behavior.^[9] 2) Extreme specific surface. As catalytic reactions usually take place at material surface, expanding the specific surface area by designing nanotubes, graphene and interconnected framework with various dimensions would endow the carbon materials with more exposed active sites and faster mass transfer.^[10] 3) Good corrosion resistance. The stability of performance and structure in harsh acidic/alkaline environment indicates its excellent supporting property.^[11] 4) Economical price. Carbon sources are easily obtained from nature, suggesting low cost and bright prospects for large-scale production.^[12]

Besides above inherent properties of carbon materials, defects inside are demonstrated to play a crucial role in electrocatalysis. Recent studies assert that the electrocatalytic activity originates from the broken integrity of π conjunction,^[13] which draw our attention back to the intrinsic property of defective carbon configuration. Basically, it is believed that the positively charged C (δ^+) adjacent to electron-withdrawing atoms or functional groups would benefit the adsorption of O₂ and OOH* in ORR, and promote the OOH* formation from O* through optimizing adsorption energy in OER,^[14] which are often considered as the rate-determining steps in the inverse reactions, respectively.^[14,15] Through defect engineering strategies, it is possible to achieve the modulation of electron structure then to controllably tune the corresponding electrocatalytic activity and selectivity. In this review, we provide a

brief summary of defective carbon-designing way for OER and/or ORR, including intrinsic and extrinsical defects as well as relevant characterization methods. In addition, the structure-performance relationship for the bifunctional oxygen electrocatalysis is deeply discussed based on the microscopic structure of the electrocatalysts. Finally, we proposed the current challenges and prospective development direction, which might provide some instructions in Zn-air battery fields.

2. Types and Characterization of Defective Carbon Materials

According to the second law of thermodynamics, the intrinsic carbon defects are inevitable and exist in several formations. Firstly, topological defects are frequently observed in the carbon nanomaterials. Lattice disorder in hexagon network often occurs, leading to the carbon rings of pentagons, heptagons, octagons, and pentagon-heptagon pair (Stone-Wales defect).^[16] Secondly, vacancy defects (single/multi) and basal holes are intensively reported. The catalytic behavior would be optimized due to the exposure of more sites and it is facile for those defects to anchor foreign atoms or functionalization.^[17] Finally, edges are considering as another type of defects in carbon nanomaterials. It is demonstrated that rich edges could exhibit higher ORR activity than basal carbon atoms, for the electronic structure at edges are similar to doping sites.^[18] Till now, it is hard to tune the topological defect by designing way, while the latter two have been achieved successfully through hole-generating approach such as chemical drilling^[19] and plasma,^[20] or down-sizing methods to expose more edge sites like ball-milling.^[21] Generally, the extrinsic defects are introduced by heteroatom-doping way, including nonmetallic atoms like N,^[22] P,^[23] B,^[25] S^[26] and metallic atoms,^[26] in which transition metal are increasingly popular due to a bunch of advantages such as low cost and high activity.



Sidi Wang received her B.S. degree from Donghua University in 2016. Now she is a master candidate in University of Science and Technology of China. Her research focuses on carbon-based electrocatalysts for oxygen reduction/evolution.



Hongliang Jiang received his Ph.D. in East China University of Science and Technology in 2016. Currently, He is a Research Associate Professor in University of Science and Technology of China. His research interests focus on controlled synthesis, mechanism studies, and electrocatalytic applications of non-noble metal nanomaterials.



Li Song received his Ph.D. in 2006 from Institute of Physics, Chinese Academy of Sciences (advisor SiShen Xie). After four years as postdoctoral researcher at University of Munich Germany and Rice University USA, he became an associate professor at Shinshu University in Japan. He was promoted to professor at University of Science and Technology of China in 2012. His current research interests are synchrotron radiation study of low dimensional nanostructures and energy-related devices.

comparable to noble metals. Schematic diagram for types of defective carbon materials is shown in Figure 1.

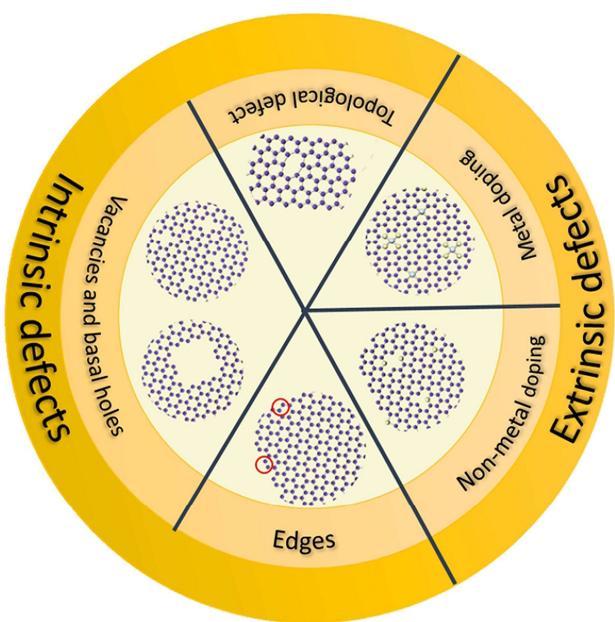


Figure 1. Types of defective carbon materials.

Defect investigation benefits from the development of electron microscope (for direct observation) and spectroscopy characterization (for indirect calculation and analysis). Aberration correction in scanning transmission electron microscopy (STEM) provides a great enhancement of resolution without raising the acceleration voltage, and the corresponding signal receiver of annular dark field (ADF) are widely used in defect detecting.^[17d] Moreover, connecting STEM with energy disperse spectroscopy (EDS)^[27] or electron energy loss spectroscopy (EELS)^[28] could achieve element identification at defects even in sub-angstrom scale.^[29] What's more, X-ray absorption spectra (XAS), including both near edge structure (XANES) and extended X-ray absorption fine structure (EXAFS), plays an increasingly significant role in distinguishing doping defects toward oxidation states, geometric configuration and binding condition.^[30] Brunauer-Emmett-Teller (BET) analysis based on N₂ adsorption isotherm data can suggest the amount of edge or pores to a certain degree,^[31] which correlates to the catalytic efficiency. The G and D peaks in Raman originate from in-plane vibration type and in-plane breathing vibration mode, respectively, and the relevant I_D/I_G value represents the disorder degree of carbon structure.^[32]

2.1. Dopant-Free Carbon Materials

In light of the discovery that the charge redistribution originates from the broken integrity of carbon framework, it is rational to believe pure carbon with defects has decent electrocatalytic activity.^[17d,33] A typical work reported by Hu and

his coworkers was pure carbon nanocages synthesized by charring the benzene with in situ MgO template method followed by acid treatment.^[17a] As calculated by BET method, the sample prepared at 700 °C possessed the highest specific surface areas, 1713 m² g⁻¹. Meanwhile, the HRTEM images and the extreme I_D/I_G value indicated abundant defects at corners, broken fringes and holes (Figure 2a-c), providing massive active sites for ORR. Other morphologies are also carried out for defective carbon-based electrocatalysis. For example, Dai and coworkers designed the dopant-free graphene with rich defects and edges by plasma etching (Figure 2d).^[20a] As shown in Figure 2e, many nanosized holes on basal graphene could be seen in HRTEM image. The defects were also detected by the increasing value of I_D/I_G in Raman and higher percentage of sp³ carbon peak in XPS. To verify the universality of introducing adequate defects by plasma treatment, few-layer carbon nanotubes were also introduced and obvious cracks on the tubular structure could be observed (Figure 2f). Similar result was reported in Waki's work where multi-walled carbon nanotubes with hole defects on the walls were synthesized by strong acid treatment of annealed nanotubes and followed chemical drilling though Co impregnation (Figure 2g).^[34] From the monochromated TEM and HAADF images, we can clearly see the holes and edges of the main sample existing from the outer walls to the center. For edge defects, Shui et al. unzipped the outer walls of multiwall carbon nanotubes (MWCNTs) to achieve zigzag-edges,^[35] the great performance for ORR of which was demonstrated by extensive researches.^[15,17a,21] Suenaga and coworkers observed Stone-Wales defect by HRTEM directly, which fitted the simulation model very well (Figure 2h and 2i).^[36]

2.2. Nonmetallic Doping

2.2.1. Mono-Atom Doping

In order to further modify the electronic structure of the nanocarbon materials, foreign atoms are generally introduced including aforementioned B, N, O, S and P. According to recent studies,^[37] carbon materials doped by halogen elements (F, Cl, Br and I) showed great potentials on ORR and OER as well. The corresponding dopant content detected by XPS is usually below 8 at% (N),^[38] and because of lattice mismatch, the value for other non-metals is relatively lower.^[24a,39] However, the doping content is not the only factor that has effects on the electrocatalytic property. Doping element, doping location and dopant distribution all influence the final catalytic performance. Among all the heteroatoms, nitrogen is regarded as the most popular dopant compared to other foreign atoms. Generally, pyrolysis is introduced to synthesize N-doped carbon materials, including one-pot calcination in inert atmosphere with C and N sources (like cyanamide, dicyanodiamide, melamine and corresponding polymer-g-C₃N₄),^[30b,c,40] or annealing as-prepared graphene oxide in NH₃ flow in which ammonia molecule can react with O-containing groups for the formation of C–N bonds.^[41] The existing formations of N elements are among pyridinic N,

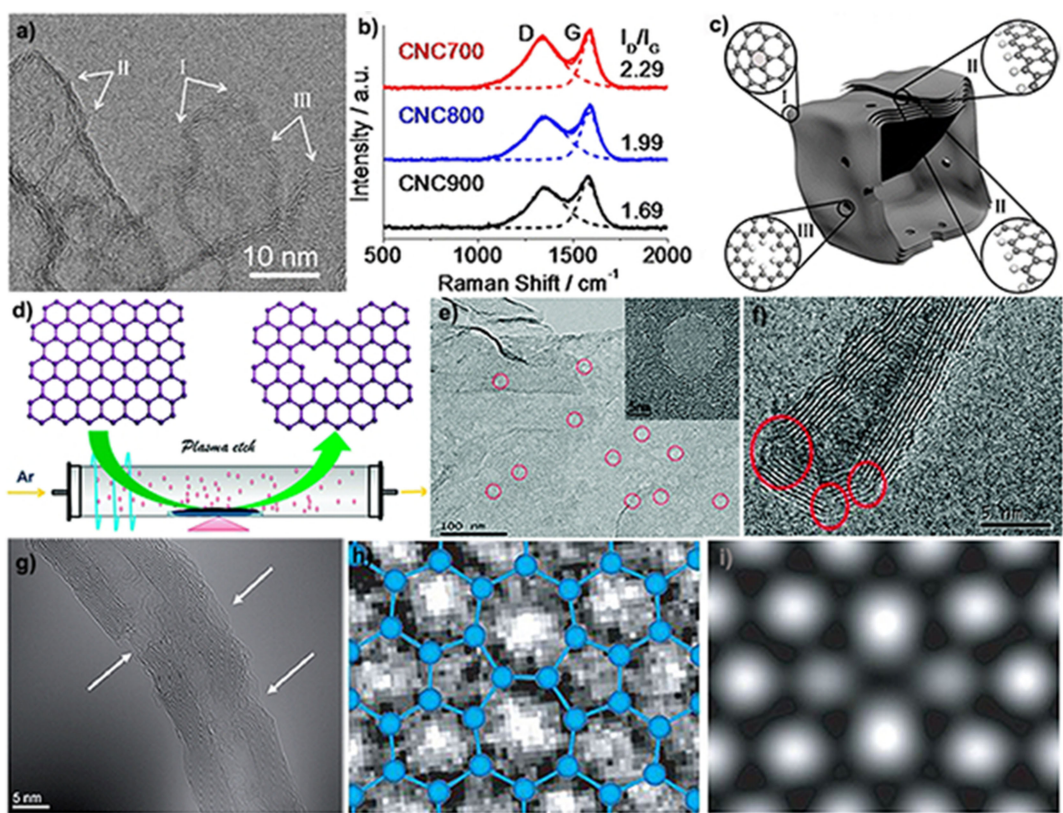


Figure 2. a) HRTEM image of the carbon nanocage annealed at 700 °C. b) Raman results of samples annealed at different temperatures. c) Schematic structure of the nanocage and various defect types. Reproduced with permission.^[17a] Copyright 2015, American Chemical Society. d) Schematic illustration of the preparation of defective graphene by plasma treating. TEM image of the defect-rich e) graphene and f) carbon nanotube. Reproduced with permission.^[20a] Copyright 2016, Royal Society of Chemistry. g) Monochromated TEM images of drilled defects on walls of DMWNT. Reproduced with permission.^[34] Copyright 2014, Royal Society of Chemistry. h) HRTEM image of Stone-Wales defect and i) corresponding simulated illustrate. Reproduced with permission.^[36] Copyright 2007, Nature Publishing Group.

pyrolytic N and graphitic (quaternary), but the activity attribution is still ambiguous.^[40,42]

To endow metal-free carbon materials with porous structure, metal/metal oxides are usually taken as templates and then removed through acid treatment.^[43] For example, Wei et al

designed N-doped graphene mesh by a template-etching method (Figure 3a).^[13c] In this work, sticky rice was taken as biomass carbon source because the gelatinized rice can bond strongly with inorganic Mg(OH)₂ template as well as permeate uniformly. In pyrolysis process, water vapor was released in-situ

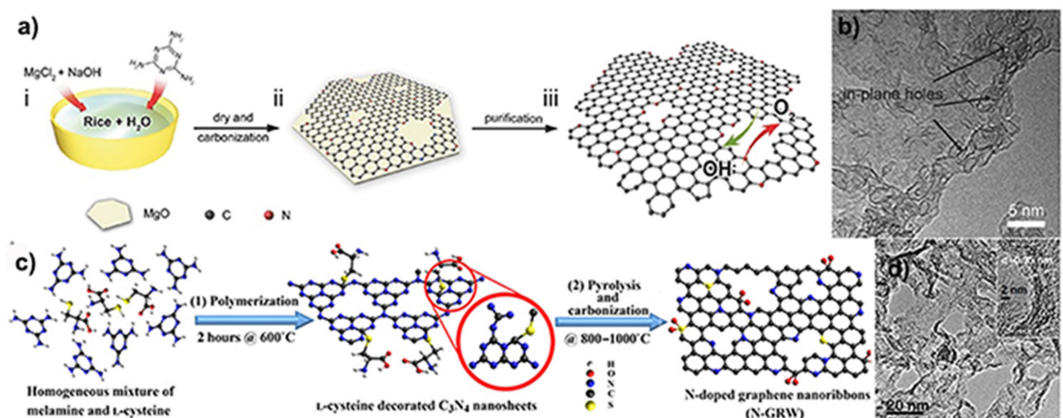


Figure 3. a) Illustration of the fabrication of NGM by sticky rice. b) HRTEM characterization of graphene layer with porous structure. Reproduced with permission.^[13c] Copyright 2016, Wiley-VCH. c) Schematic of preparation steps and d) high-resolution TEM image of 3D interconnected structure of N-GRW. Reproduced with permission.^[40] Copyright 2016, the Authors, some rights reserved; exclusive licensee American Association for the Advancement of Science.

thus formed rich macro holes on the substrate homogeneously (Figure 3b). Dominant sp^2 -hybridized C–N configurations were identified through nitrogen K-edge EELS spectra where the graphitic and pyridinic N corresponds to σ^* bonds with different shapes and positions.

For the purpose of feasibility and energy efficiency, it is desirable to design metal-free catalysts with self-templates even no templates.^[30b,44,45] Taking it as a principle, Dai et al developed N-doped 3D nanoribbons by L-cysteine and melamine as carbon and nitrogen source, respectively.^[40] As shown in Figure 3c, the raw materials were mixed and grounded with a specific ratio to be homogeneous, followed by the subsequent polymerization at 600 °C. As a result, L-cysteine was covalently bonded with g-C₃N₄ via thiol groups that played an important bridging role due to the high activity. Therefore, in the next pyrolysis process at a higher temperature under argon atmosphere, the newly formed carbon nitride not only provided adequate N atoms but also as a template for the final interconnected nanostructure with porous morphology (Figure 3d). Massive defects generated in the two carbonization steps as the I_D/I_G ratio was up to 3.34 and the specific surface increased to 530 m²g⁻¹, much higher compared to the intermediate products and control samples.

With similar atom diameter and better O₂ absorption property compared to C, boron arouses great interests as a dopant as well.^[24b] Most reported B-doped graphene was synthesized by chemical vapor deposition (CVD) method,^[46] while Pattanayak et al. used the epitaxial graphitization technique by B₄C to design few-layered B-doped graphene.^[24c] Briefly, B₄C, as both C and B source, underwent a heat treatment at above 1400 °C in inert atmosphere (Figure 4a). In the case that graphene is hydrophobic while B₄C has hydrophilic nature, phase-separation was easily carried out by a feasible water-based treatment method (Figure 4b). The graphene purity was confirmed by XRD compared with the B₄C crystals. Then,

equally spaced bands on both sides of central peak in ¹¹B solid state NMR spectrum indicated the existence of B atom in carbon lattice, and co-presence of π and π^* peaks at B edge in EELS gave the evidence of the sp^2 doping formation of B defects.

S and P with much larger sizes can introduce more strain and defects to carbon materials, thus attracted numerous attention even if S has similar electronegativity with C. To exclude the effect of metal impurities, CVD method is replaced while the alternatives such as treating pristine graphene or CNT in S/P-containing species atmosphere at high temperature are developed recently.^[23b,c] For example, Yang and co-authors attempted a P-doped carbon hollow spheres by hydrothermal-annealing method,^[47] taking glucose, tetraphenylphosphonium-bromide (C₂₄H₂₀P(Br)⁺), sodium dodecyl sulfate (SDS, CH₃(CH₂)₁₁OSO₃Na) as C source, P source and soft template, respectively (Figure 4c). In the first process, SDS formed micelles spontaneously with polymerized glucose interweaving, while positively charged C₂₄H₂₀P(Br)⁺ and SDS anion jointed with each other by electrostatic attraction, which both contributed to the whole structure of the precursor. The template decomposed at the final pyrolysis step, then a hollow sphere with high exposed interface was constructed. Both FTIR and XPS spectra directly pointed out the existence of P–C bonding, indicating the P atom incorporated into C lattice as a defect.

2.2.2. Dual Doping

Co-doping in carbon lattice with two foreign atoms is considered as an increasingly popular way to optimize the catalytic activity for it can create a synergistic effect to promote the electrocatalytic activity. Various doping modes, especially N associated with other heteroatoms like N–S,^[48] N–O,^[49] N–B,^[50] N–P^[51] are widely reported. For instance, taking advantage of t-

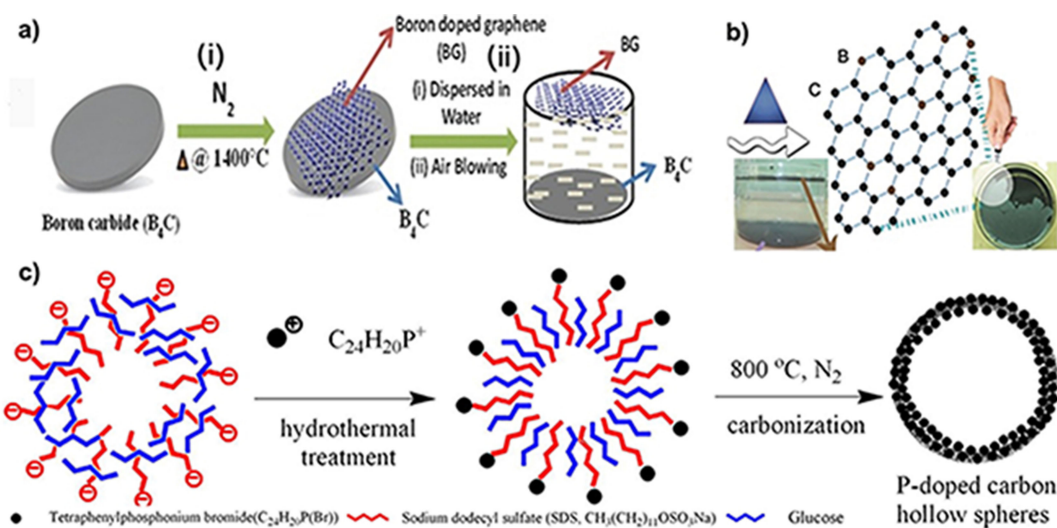


Figure 4. a) Preparation of B-doped graphene separated from bulk B₄C. b) The great difference in density between two phases makes it easy to obtain graphene. Reproduced with permission.^[24c] Copyright 2015, Wiley-VCH. c) Illustration of the synthesis of P-doped carbon hollow spheres.^[47] Copyright 2015, Elsevier Ltd.

carageenan extracted from seaweed with S element, Yao and co-workers designed a S, N co-doped carbon aerogel (Figure 5a).^[16a] Urea as N source, a hydrogel was formed at room temperature after gelation at 80 °C. To gain porous aerogel NSCA-700, the freeze drying, pyrolysis and an acid treatment were carried out on the precursor in order. X-ray absorption structure (XAS) showed the existence of oxidized S and disulfide at this stage, but a transformation to thiophene S^[52] occurred after final annealing at 1000 °C (Figure 5b). It is also found that graphitic N predominated in NSCA-700-1000, with pyridinic and pyrrolic N decreasing dramatically. At the C K-edge XAS spectra, two peaks at 283.7 and 284.3 eV were ascribed to C defects in carbon lattice, which was verified in STEM and its filtered images with distinct pentagon defects (Figure 5c).

Besides top-down methods, bottom-up synthetic ways are also welcome because using prepared graphene or CNTs as precursors could dramatically reduce the formation of amorphous carbon in pyrolysis procedure.^[53] A representative work was reported by Qiao et al.,^[54] where a N, O dual doping graphene-carbon nanotube hydrogel film (NG-CNT) was elaborated through the layer-by-layer assembly way (Figure 5d). The films were obtained by suction filtration from homogenous mixture of GO and CNTs, followed by ammonium hydroxide treatment for N doping. On the contrary, O atoms were the residual impurities introduced by initial graphene chemosynthesis. Indicated by an evident growth of $\pi^*(C=O)$ peak intensity in XANES compared with N-doped graphene, it is concluded that the sandwich-like structure of NG-CNT had strong interaction between the two components, implying good conductivity. Further, an amount of N atoms (~9.9%) in formation of pyridinic and pyrrolic N meant massive defects and active sites.

Although some mono-doped carbon materials show good electrocatalytic activity, it is not necessary for the corresponding dual-doped samples to achieve better performance. Besides the effect of dopant type, the microstructure also plays a crucial role. Hu et al pointed that bonded B and N dopant pair could not break the inert property of CNTs, while the separate doping mode endowed the electrocatalyst with excellent ORR performance.^[55]

2.2.3. Multi Doping

Ternary doping also attracts considerable attention from researchers since Woo has reported a N, B and P co-doped carbon material.^[56] He suggested the synergistic way that P improved charge delocalization and generated plenty of edge defects, while B increased the pyridinic-N portion and strengthened sp² framework. P, N and S ternary doped carbon was designed by electrostatic assembly with sequent pyrolysis where C₂₄H₂₀P(Br) and (NH₄)₂S₂O₈ were taken P, C source and N, S source, respectively. Thiophene-S and three types of N was detected by XPS analysis, and notably, P bonded with N as well except for P-C bonding. All the PNS-PCs showed bad crystallinity, and PNS-PC-2 with higher P content even manifested amorphous property, indicating a great amount of defects internally.

2.3. Metallic Doping

Metal modification is demonstrated to have significant effects on defective carbon materials as trace amount of metal impurity could dramatically enhance the catalytic activity,^[11a,57]

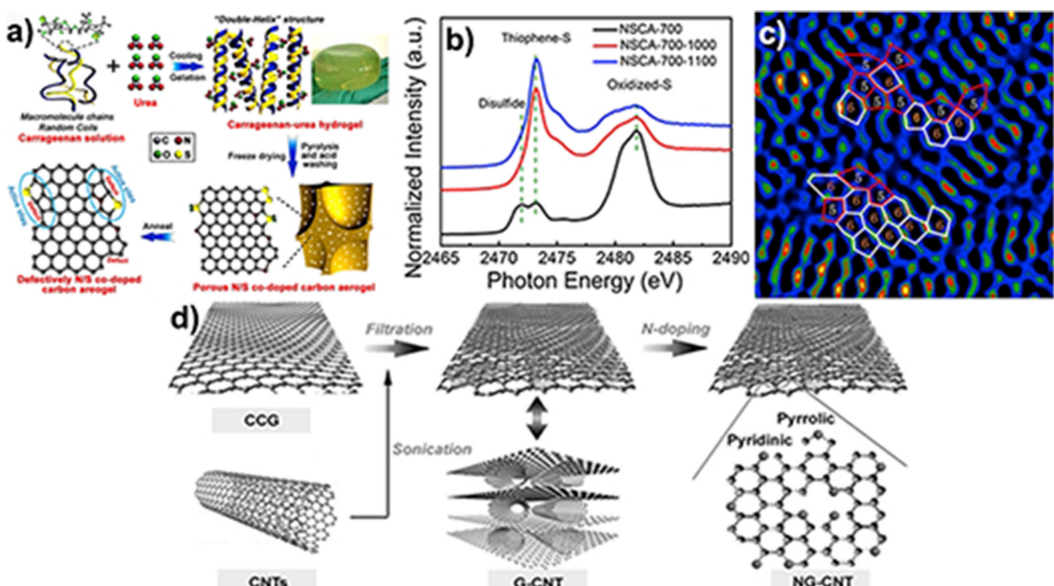


Figure 5. a) The preparation process of N and S co-doped carbon aerogel. b) XAS spectra of NSCA-700, NSCA-700-1000, and NSCA-700-1100 at S K-edge. c) STEM image of NSCA-700-1000. Reproduced with permission.^[16a] Copyright 2018, Elsevier Ltd. d) Schematic of fabrication of NG-CNT. Reproduced with permission.^[50] Copyright 2014, Wiley-VCH.

while being an obstacle for the investigation of metal-free electrocatalysts in previous years. On the contrary, the advantage of metals could be fully taken by ingeniously designing the geometric and electronic structures of efficient catalysts.

In order to make better use of the noble atoms and reduce the cost, decreasing the nanoparticle size is acclaimed for marked enhancement could be achieved after down-sizing.^[58] Of special interest is the single-atom catalysts (SACs) that combines the merits of homogeneous and heterogeneous catalysis, and touches the limit in availability factor.^[26,53] Defective carbon-based SACs are introduced for a number of electrocatalytic reactions like ORR, OER and HER.^[26,59] The strong interlinking between metal atoms and the support could facilitate the charge transfer, stabilize the atomically dispersed structure and affect the reactive performance. This way offers the possibility to tailor the catalyst's structure at nanoscale.

As widely reported, M–N–C (M=Fe, Co, Ni, Mn, etc) SACs could possess comparable catalytic activity to noble metal-based electrocatalysts,^[60] giving rise to enormous attempts on them. To prevent the thermal aggregation, the metal loading should not be very high. On the basis of recent reports, the content of 4.0 wt% (<1 at%) seems the limit value,^[61] which is usually measured by Inductively Coupled Plasma (ICP) or mass spectrometer (MS). Therefore, the synthetic process is usually designed elaborately such as selecting eligible precursors or tailoring experimental methods. Component-tunable metal organic frameworks (MOFs) are frequently taken as the precursors.^[62] In a highly cited work accomplished by Li et al.,^[61b] the Co–N–C single-atom ORR catalyst was designed through a bottom-up strategy with Co/Zn bimetallic MOF as precursor

(Figure 6a). In the process of MOF synthesis, Zn acted as a “fence” to control Co growth spatially. In the pyrolysis, Zn atoms evaporated away due to low boil point leaving more N sites while Co was reduced by generated carbon and atomically trapped in N-doped defects that were inherited from N-containing organic linkers. The Co valence in single-atom sample was between 0 and +2, deduced from the position of white line peak between Co foil and MOF precursor in the XANES spectra. Single atoms were observed by HAADF-STEM images (Figure 6b–6d), and the absence of Co–Co binding in Fourier transformed (FT) EXAFS curve in R space verified that single atom was the only existing formation of Co element. Dual metal-doping engineering could also be achieved by taking the advantages of MOF materials. For instance, Yao and co-workers designed a defect-rich hollow nanostructures with atomic Co–Pt coupling was by an artful way, shown in Figure 6e.^[63] Co–MOF as the precursor, a core-shell sphere (Co–NC) was constructed through carbonization with Co metal inside and N-doped carbon coating outside. Finally, electrochemical activation was introduced, taking Pt wire as the counter electrode. In this process, partial amorphous carbon with unstable property corroded and generated interstices for acid entering and ions escaping. The newly emerged lattice defects as well as dangling bonds, seized the chance to capture Co and Pt ions, which could be deduced from the concentrated distribution of single atoms at the openings of the graphitic shell. HAADF image showed the local coordination conditions around Pt and Co atoms, and an interesting coupling configuration of two atoms trapped in N-doped carbon defects was found (Figure 6f), which was also confirmed by following

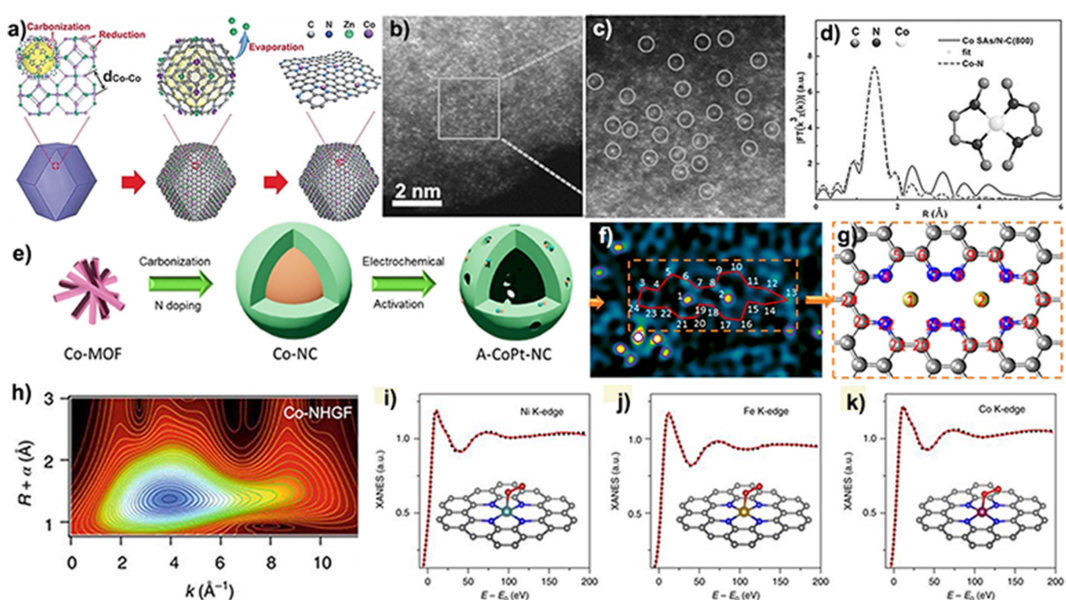


Figure 6. a) Formation of Co SAs/N–C by MOF as the precursor. b) The characterization of single atoms by HAADF-STEM and d) magnified image show only atomically dispersed Co exist in the sample. d) EXAFS fitting result of Co SAs/N–C(800) indicates the Co–N₄ structure. Reproduced with permission.^[61b] e) Schematic of preparation procedure of A-CoPt-NC. f) Corresponding FT-HAADF image. The yellow and cyan dots represent metal atoms, respectively, and area surrounded by red line is simulated in g). Two metal atoms are trapped in the vacancy. Reproduced with permission.^[63] h) Wavelet-transformed k^3 -weighted EXAFS curve of Co–NHGF at 2.0 Å. Excellent matching between experimental and theoretical XANES results of i) Ni–NHGF, j) Fe–NHGF and k) Co–NHGF. The insets are the best-fitting MN₄C₄ configurations. k) ADF-STEM image of Fe–NHGF directly gives the geometric structure of FeN₄C₄. Reproduced with permission.^[53] Copyright 2018, Nature Publishing Group.

theoretical calculating (Figure 6g). The pre-edge peak at 7712 eV of Co XANES spectra suggested Co-N₄ square-planar geometry, while Pt–N and Pt–C, or Co–N and Co–C in EXAFS were hard to distinguish due to their close peak position, which is common in all the relative study and further curve fitting should be introduced.

A recent work by Duan et al explicitly exhibited the application of XAS in SACs.^[53] A series of atomically dispersed M–N–C (M=Ni, Co, Fe) OER catalysts were synthesized by a general gelation-pyrolysis strategy. The carbon source was graphene oxide (GO) possessing rich defects, which would be favorable to producing intrinsic defects, binding N atoms or anchoring metal atoms. H₂O₂ also played a significant role in generating holes on graphene plane in the hydrothermal treatment. To explore the exact coordination condition of the absorbing center, they analyzed the XAS results intensively. 1) In FT-EXAFS, the signals in the three M-NHGFs were evidently different, and each main peak with shorter distance compared to their corresponding M–O was ascribed to backscattering between metal and light atoms. 2) In EXAFS wavelet transform (WT), it was concluded that the metal existed as mononuclear center in the whole system rather than crystalline as the only intensity maximum was located at 4.0 Å⁻¹. Then, the MN₄C moiety was validated in the following EXAFS-WT curve-fitting resolution in both k and R space (Figure 6h), based on the results of dominant contribution of M–N and calculated coordination number. 3) In XANES spectroscopy, the valence state and refined atomic-site structure were confirmed by a range of simulations and analysis. Single metal atoms existed in the center of graphene divacancy, incorporating four pyridinic N atoms from six-member carbon rings and being embedded in carbon lattice. XANES fitting is a powerful tool to predict the metal–carbon configuration structure and O₂ absorption situation, which significantly influence ORR performance.^[64] Herein, axial oxygen absorption state was further revealed to achieve near-perfect agreement between calculation and experiment (Figure 6i, 6j and 6k). In addition, ADF-STEM images unambiguously exhibited the defect configuration, which were totally in accordance with previous characterization.

Carbon defect-supported SCAs without other nonmetal atom doping have attracted researchers' attention recently.^[65] It is possible to achieve various functions by slightly tuning the coordination condition and electronic structure in the same system. Yao et al designed defected graphene-Ni single-atom catalyst with impregnation technique and subsequent acid treatment without other nonmetal-atom coordination.^[66] Taking advantage of HAADF-STEM, extremely clear difference between vacancies or dopants and ordered lattice was shown by brightness comparison. Further, double vacancy in graphene could be seen directly and the bright dot indicated Ni atom were trapped into the defect center in the zoom-in view. Combining XANES and FT EXAFS spectra, we could assure that all Ni atoms were atomically dispersed in graphene with different Ni–C coordination environment.

3. Relationship Between Defect Structure and Bifunctional Activity

To evaluate the electrocatalytic performance of ORR and/or OER, several criteria are introduced in which the overpotential measured by linear sweep voltammetry (LSV) or cyclic voltammetry (CV) is of great importance. The ideal scenario (zero overpotential to equilibrium potential) is hard to occur due to the chemisorption energy of intermediates.^[67] Tafel slope, a kinetics parameter, calculated by LSV results reveals the level of difficulty for startup and the rate-determining step in some way.^[68] 4e⁻ transfer is considered the most efficient pathway, and the corresponding electron transfer number is obtained by Koutecky-Levich plot or LSV results tested by rotating ring disk electrode (DDRE). ΔE, the voltage gap between half-wave potential (E_{1/2}) in ORR and the potential (E₁₀) in OER when current density is 10 mA cm⁻², is an important indicator to evaluate bifunctional performance. Finally, the bifunctional catalysts are usually assembled into a whole air-metal battery as cathode to assess the service performance since electrical loss would occur at assembly interface, different from electrochemical tests. What's more, cycle stability also plays a crucial role in performance evaluation system.

The enhancement in catalytic behaviors may be ascribed to increased amount of active sites by expanded surface area or electrochemical active surface area (ECSA),^[10] updated dopants or improved conductivity, while these analysis is far from enough. For this purpose, the density functional theory (DFT) calculation could investigate the electronic structure and geometric configuration of real active sites, as well as the reaction dynamics in catalytic process, then effectively instruct the catalyst designing in the future. The charge density map shows the distribution situation of electrons and holes at the interface of two phases^[69] and Bader analysis provides the exact amount of charge at and around the doping site of heteroatoms to confirm the real active site.^[70] Besides the information of the property on electricity conducting, density of state (DOS) at Fermi energy can also identify the contribution of a specific atom, indicating the active sites since higher density is usually more beneficial for molecule adsorption.^[71] Moreover, the kinetics information and the rate-determining step (rds) can be provided by free energy diagram calculated by intermediate absorption energy with the reference of standard hydrogen electrode (SHE). Nevertheless, the electrocatalytic process of OER/ORR is very intricate, involving mass transfer, electron conduction, and surface redox. Therefore, despite of enormous efforts on characterization and the first-principles, the catalytic mechanism is still ambiguous as no unanimous catalytic mechanism could be concluded for different materials and synthetic process.

3.1. Metal Free

As we discussed above, the doping defects in carbon materials could generate charge redistribution and activate the catalytic

capability. As massive reports, some metal-free bifunctional oxygen electrode may surpass the counterpart containing metal atoms.^[72]

Without deliberate O-doping, Wang exfoliated the carbon cloth (CC) by Ar plasma treatment and exposed it in air to get rich edge defects and O-containing functional groups.^[20b] Compared with pristine CC, plasma-treated P-CC possessed much better OER activity with 10 mA cm^{-2} at 1.68 V, and 70 mV higher onset potential of ORR in 0.1 M KOH solution. O-groups and specific surface area both contributed to the great property. According to the volcano plots of DFT results, defective graphene with C-OOH had the minimal overpotential for both OER (0.39 V) and ORR (0.41 V) (Figure 7a and 7b), which was even better than RuO₂ (0.42 V) and Pt (0.45 V), respectively. Based on the charge transfer analysis, the carbon atoms adjacent to C=O or C—OOH would be electron-deficient due to charge redistribution, then became positively charged as the possible active sites to absorb and catalyze reactants (Figure 7c).

In N-doped material system, the C atoms adjacent to N is well believed as the active sites by extensive experimental and theoretical studies.^[73] However, the N types contributing to OER/ORR are in serious disagreement, especially for pyridinic N and quaternary N. Reported by Liu and coworkers,^[40] N-doped nanoribbon (N-GRW) with abundant edges exhibited outstand-

ing bifunctional performance with 0.92 V of onset potential for ORR and 0.36 V overpotential at 10 mA cm^{-2} for OER in 1 M KOH. The low work function (Φ) of N-GRW implied small energetic barrier for O₂ absorption (Figure 7d), which was considered as rds in this study. Using Φ to explain the electrocatalytic performance was also reported by some other works.^[74] The catalytic mechanism was investigated by XANES characterization technique (Figure 7e and 7f). Comparing the peak changes before and after OER, ORR reactions, they verified the quaternary N (n-type) atoms at edges contributed to ORR, while pyridinic N (p-type) was responsible to OER, originating from the changes of peak position. N-GRW taken as air electrode, a two-electrode Zn-air battery was carried out with high peak power density (65 mW cm^{-2}), specific capacity (873 mAh kg^{-1} Zn), and good cycle stability, comparable with Pt/C+Ir/C.

Other nonmetal-doping carbon materials, like B doped CNTs or graphene were reported to have OER and ORR behaviors simultaneously, but the authors did not mention the catalytic mechanism or no more than ORR explanation.^[24b] Likewise, no mono P-doped carbon materials with bifunctional capability were stated as we know. Nonetheless, dual or multi-doped metal-free carbon are widely investigated by virtue of the synergistic effect.^[30c,72]

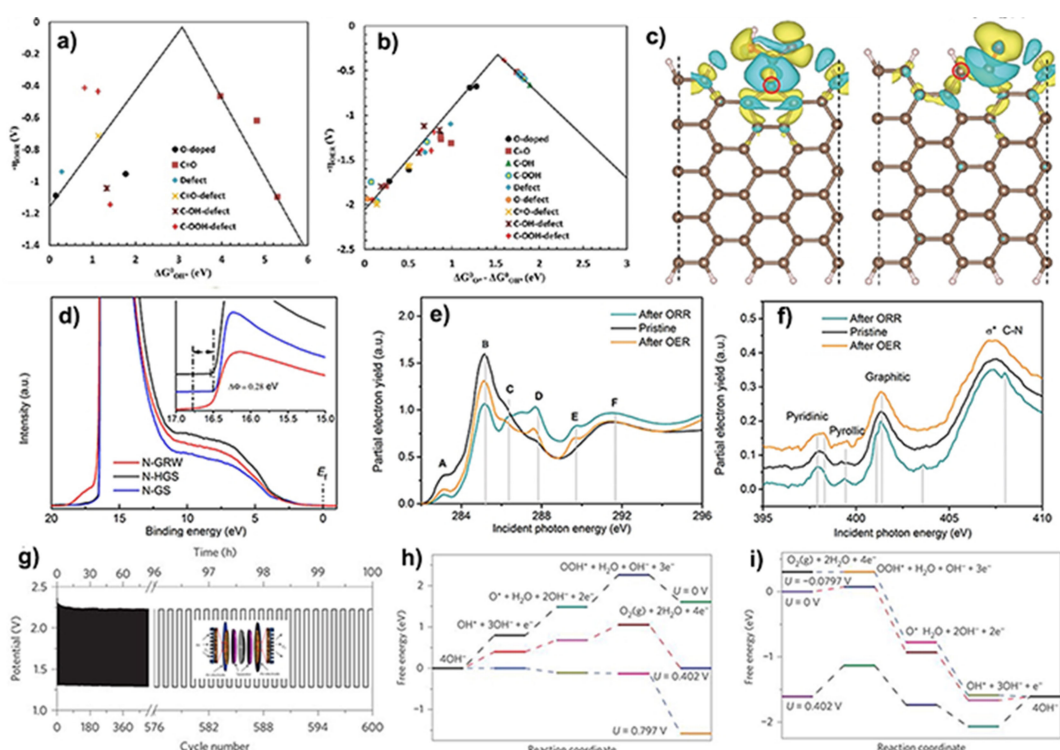


Figure 7. The volcano plots on different defects of the nanofiber in a) ORR and b) OER. c) Charge density distribution on armchair graphene with C-OOH (left) and C=O (right). Blue and yellow represent positive and negative charge, respectively. Red circles indicate the most active sites. Reproduced with permission.^[20b] Copyright 2017, Wiley-VCH. d) UPS signal obtained by He I (21.2 eV) radiation. The inset provides the zoomed-in field of secondary electron tail threshold. The XANES spectra of N-GRW at K-edge of C e) and N f) before and after ORR and OER. A, B, C, D, E, F indicate defects, p* \equiv C, p* \equiv C—OH, p* \equiv C—O—C or C—N, p* \equiv C=O or COOH, s* \equiv C—C, respectively. Reproduced with permission.^[40] Copyright 2016, the Authors, some rights reserved; exclusive licensee American Association for the Advancement of Science. g) Cycle stability of charge-discharge for Zn-air battery with NPMC-1000 as oxygen electrode at 2 mA cm^{-2} . Inset is the schematic configuration of corresponding three-electrode system. Elementary reactions of OER h) and ORR i) for N, P co-doped graphene in alkaline electrolyte. Reproduced with permission.^[67b] Copyright 2015, Nature Publishing Group.

Dai synthesized N, P co-doped mesoporous carbon material by polymerizing aniline monomers in the presence of phytic acid, followed by a pyrolysis process.^[67b] In 0.1 M KOH solution, great ORR performance of NPMC-1000 was obtained with onset and half-wave potential of 0.94 V and 0.85 V vs reversible hydrogen electrode (RHE), respectively, comparable with commercial Pt/C. Although NPMC-900 possessed higher N and P doping content, insufficient graphitization degree would decrease the conductivity. However, overheating would also be inadvisable as the high temperature could destroy the N, P dopant structure. Four-electron process was confirmed by double insurance (i.e. K-L plot and RRDE measurement), indicating an efficient reaction path. DFT calculation showed that N, P-coupled dopants rather than the isolated N or P sites had lower overpotential, highlighting the importance of synergistic effect of N, P co-doping. Taking NPMC as the air cathode to assemble a Zn-air battery, we can see a series of great performance including open-circuit potential (OCP) of 1.48 V, peak power density of 55 mW cm⁻², and specific capacity of 735 mAh kg⁻¹ Zn, further suggesting good ORR performance of the applied catalysts. The low charging potential indicated a relatively high catalytic activity towards OER (Figure 7g). Additionally, the negligible change of charging/discharging potential, and small voltage gap indicated the satisfactory stability and rechargeable battery performance due to the efficient bifunctional oxygen electrocatalysis (Figure 7g), evaluated by a three-electrode system that separated the two electrodes in order to impede the cathode being oxidized in ORR and reduced in OER. The elementary steps in OER and ORR were provided through theoretical calculation in Figure 7h and 7i.

3.2. Metal Containing

SACs make the most use of metal atoms by elaborately designing the metal-support coordination configuration in order to reduce the dopant amount and the corresponding cost. Of great consideration in noble metals is Pt based SACs, while they are reported easily trapped into high H₂O₂ production problem in ORR process,^[75] and thus M–N–Cs are highly ionized owing to comparable catalytic property. However, most M–N–Cs have ORR performance while the OER-favorable counterparts are rarely reported. Wu reported a bifunctional single-atom S,N–Fe/N/C–CNT,^[76] in which S doping increased the specific surface area and facilitated the Fe impurity dissolving. A small ΔE (0.75 V) between ORR and OER electrocatalysis suggested efficient bifunctional oxygen catalysis (Figure 8a). When applied as the electrode material in Zn-air battery, the open circuit voltage is similar with that of Pt/C catalyst, implying a good catalytic performance toward ORR (Figure 8b). The high maximum of power density (102.7 mW cm⁻²) was even higher than that of Pt/C catalyst (Figure 8b), which is attributed to efficient charge transfer and improved accessibility of electrolyte as well as oxygen species in the single-atom S,N–Fe/N/C–CNT catalyst. In addition, excellent reusability was confirmed by little degradation after 10000 cycles.

Fe-N–Cs are deliberated as the superior candidate than other transition metals, but the Fenton reaction in ORR could destroy the battery separator made of polymers.^[77] Thereby, the research about alternatives like Ni, Co and Mn are springing up. In Duan' work,^[53] the single-atom Ni–NHGF exhibited exceptional bifunctional performance in 1 M KOH aqueous solution,

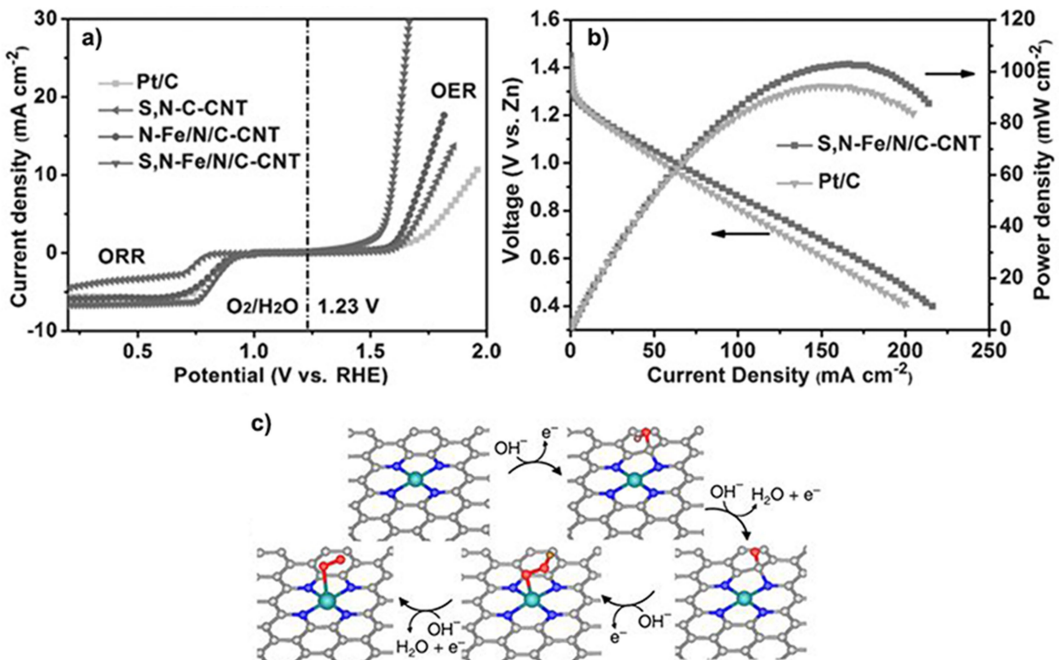


Figure 8. a) LSV curves of S, N–Fe/N/C–CNT and control samples in both OER and ORR region in 0.1 M KOH. b) Discharge polarization and power density curves for S, N–Fe/N/C–CNT and Pt/C. Reproduced with permission.^[76] Copyright 2017, Wiley-VCH. c) The illustration of dual-site mechanism of Ni–NHGF towards OER. Reproduced with permission.^[53] Copyright 2018, Nature Publishing Group.

with $\Delta E=0.70$ V in which the OER and ORR activity are comparable with RuO₂/C and 20 wt% Pt/C, respectively. Notably, the TOF of Ni–NHGF for OER was obviously higher than the counterpart of some state-of-art electrocatalysts. Meanwhile, the Faradaic efficiency (~99.2%) excluded other reaction possibilities except for O₂ generation with 4e⁻. The catalytic mechanism for OER simulated by DFT calculation indicated that the Ni–N₄ moieties occupying the center of the divacancy and the C atom adjacent to doped N are the dual-site (Figure 8c). In-situ XAFS was introduced to investigate the structure change of Ni–NHGF and Ni aggregation, and the good coincidence of location and intensity between the sample before and after cycles showed the excellent stability. Based on the control experiments, it is concluded that the mass-transport was enhanced by the porous structure, benefiting from hole-defects drilled by H₂O₂. Nevertheless, the ORR reaction pathway was not provided. Moreover, the coordination number in most M–N–Cs is four, while some researchers claimed that M–N₂ is better because excessively positive charge would result to strong adsorption between intermediates and metal atoms, and thus the desorption process will be restrained according to the Sabatier principle.

As carbon materials with edge/basal defects or doped nonmetal atoms tend to have efficient ORR performance, it is rational to design bifunctional electrocatalysts by introducing some oxides, nitrides, sulfide or phosphides whose high OER activities have been demonstrated widely.^[78] For instance, Liu decorated Cu–Co bimetallic oxide quantum dot on N-doped carbon nanotubes,^[79] and the assembled two-electrode Zn-air battery showed comparable energy density to Pt/IrO₂, resulting from good conductivity and multiple exposed active sites (Figure 9a and 9b). Noticeably, the flexible property endowed it with the potential on the all-solid-state Zn-air battery as no

detectable change occurred even after a high-angle bending (Figure 9c). Similarly, Cho and co-workers investigated the Co–Ni oxide and alloy-loaded N-doped CNT,^[80] which exhibited the optimal charge-discharge performance and narrow potential gap as the cathode in the rechargeable Zn-air battery due to the efficient bifunctional ORR/OER electrocatalysis (Figure 9d and 9e).

Recently, metal sulfides have also been reported to exhibit favorable performance for ORR and OER. For example, Dai used NH₃-plasma to treat prepared Co₉S₈-graphene hybrid.^[81] Plasma contributed to generating edge defects on graphene and exposing more surface of nanoparticles, while NH₃ here was for doping in the lattice of both carbon and sulfide to modify their electronic structures. As a result, the OER and ORR performance were enhanced efficiently, and a good stability was achieved at the same time.

When it comes to designing bifunctional electrocatalysts, researchers never stop looking for a path to realize synergistic effect, in which surface and interface engineering are of great importance.^[82] Our group reported a bifunctional composite with defective carbon supporting CoP nanoparticles.^[74] As mentioned above, N-doping graphene dominantly contributed to ORR, while OER activity was ascribed to CoP species. Notably, due to the strong bonding between the load and the substrate detected by P L-edge XANES spectra, the interfacial charges redistributed, leading to the accumulation of electrons and holes on graphene and CoP, respectively, which enhanced the ORR and OER activities simultaneously. In addition, relatively low Φ indicated a small reaction energy barrier for ORR. The excellent bifunctional behavior was exhibited by a small ΔE (0.76 V) of LSV curve from ORR to OER region in alkaline solution, implying the potential application in metal-air batteries. Recently, bimetallic phosphide was demonstrated to

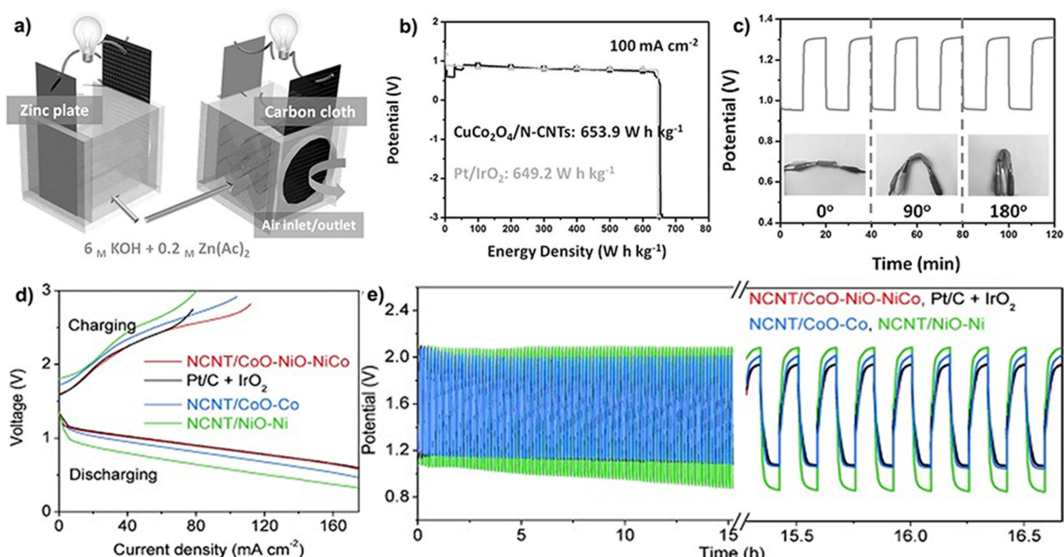


Figure 9. a) Schematic diagram of the structure of Zn-air battery. b) The gravimetric energy density of CuCo₂O₄/N-CNTs and Pt/IrO₂ at 100 mA cm⁻². c) Charging and discharging plot of all-solid-state battery at 1 A g⁻¹ at different bending angles. Reproduced with permission.^[79] Copyright 2016, Wiley-VCH. d) Charge and discharge polarization curve of secondary Zn-air batteries with NCNT/CoO–NiO–NiCo and corresponding reference samples as oxygen electrode at 50 mA cm⁻². e) The charge-discharge cycling plots of Zn-air batteries at 20 mA cm⁻². Reproduced with permission.^[80] Copyright 2015, Wiley-VCH.

have optimized OER performance as the electronic structure can be tuned by two metal elements. Thus, we designed a hybrid of CoMnP₄ nanoparticles and N, P co-doped graphene, possessing great bifunctional quality with ΔE of 0.75 along with good cycle durability.^[83]

In general, metal nitrides have superior conductivity thus can accelerate electron transfer to boost the electrocatalytic performance. By tuning metal ratios elaborately, Parkin et al investigated a series of solid solution nitrides supported by defective N-doped carbon nanotube (Ni_xCo_{3-x}N/NCNT),^[60] which exhibited favorable bifunctional quality and cycle stability. It was discovered that M–N bonding in Ni_{0.5}Co_{2.5}N was weakest, leading to an electron-deficient state in transition metal atoms, which could optimize the activation energy among active sites and reactants then enhance the OER activity. The valence states of both metal and N elements in ORR and OER process were recorded by XPS and in-situ Raman, in agreement with Bader charge analysis.

Despite of enormous calculation, researchers still endeavor to directly verify reaction kinetics through experiments.^[84] The disconnected results of ex situ measurements cannot investigate the exact reaction pathway, and the deviation existed between ex and in situ test results. Recently, in situ/operando Raman, XRD, Mössbauer, and XAS have been widely developed in electrocatalytic mechanism analysis,^[85] in which the last one gets particular attention. The corresponding research in terms of carbon based cathode materials mainly focuses on Fe–N–C moieties for ORR.^[86] According to Mukerjee's work,^[87] the Fe²⁺/³⁺ redox transition and the formation of new adsorption species on Fe center were detected by in situ XANES (Figure 10a) and EXAFS (Figure 10b) spectra by stepwise voltage increase, respectively, thus the importance of square-planar Fe²⁺-N₄ on the first-electron reduction was confirmed and the 2×2e⁻ reaction process was deduced as well. In situ characterization could effectively monitor the coordination or structure changes on active sites and it is believed that combining DFT simulation, it will benefit ZABs field much on investigations of electrocatalytic mechanism and designing electrode materials.

4. Summary and Outlook

Defective carbon materials act as one of ideal candidates for Zn-air batteries, mainly because that the novel defects in carbon materials including lattice distortion, vacancies, edges, and dopants could generate charge redistribution and change the electronic structure of adjacent C atoms, resulting in enhanced OER and/or ORR activity. Herein, we concentrate on two aspects. Firstly, we summarize the defect-generating way and associated characterization methods where aberration correction-electron microscope and X-ray absorption spectroscopy make great contribution to defect analysis. Additionally, the relationship between the bifunctional performance and defect structure is discussed mainly based on the DFT calculation. Combining the experiments with the theoretical simulation, the electrocatalytic mechanism will become clear and the corresponding merits can be further discovered and developed.

Despite of numerous efforts on carbon defects, some serious challenges still exist, which impedes the development of defective carbon-based ZABs.

- 1) Defect designing. Several defect types could present at a specific material so that the contribution of each site could not be identified explicitly. A fuzzy concept, "synergetic effect", is usually to explain the enhancement of OER and/or ORR performance, especially in multi-defective material systems. Therefore, controllably designing carbon materials with one-fold defect is of urgent importance. And with combining the DFT calculation, the in-deep understanding toward the relationship of structure and electrocatalytic performance would be established unambiguously.
- 2) Defect characterization. Generally, self-reconstruction of active sites would occur during redox processes, especially for OER, while traditional ex-situ characterization methods can not investigate the structure change during the reaction processes. Therefore, in-situ/operando measurements are highly desirable to shed light on the electrocatalytic mechanism. Additionally, the active sites in OER and ORR usually vary, and the cyclical high potential window in OER process would lead to the corrosion of carbon materials and

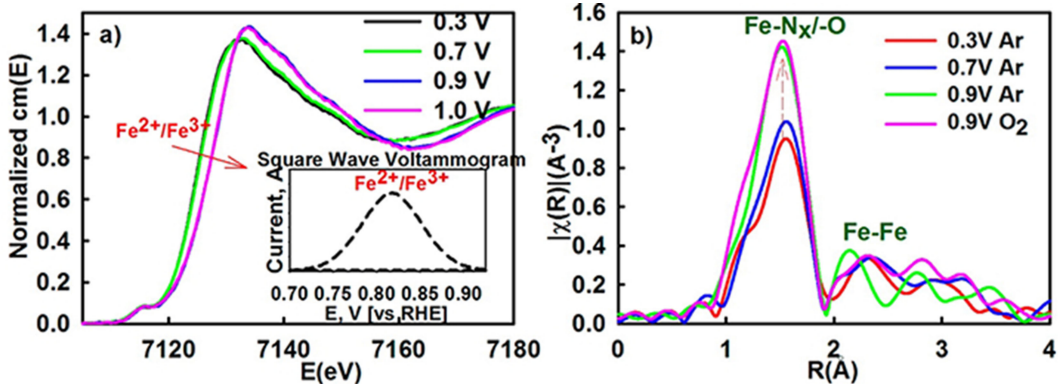


Figure 10. In situ a) XANES and b) FT-EXAFS spectra of PVAG-Fe at Fe K-edge at different potentials in oxygen-saturated/free 0.1 M HClO₄. The inset in a) is $\text{Fe}^{2+}/\text{Fe}^{3+}$ redox transition in square wave voltammogram. Reproduced with permission.^[87] Copyright 2014, American Chemical Society.

- destroy the catalytic centers for ORR. Taking use of in-situ/operando technique, one can get in-deep insight into the mechanism for performance decline, which would guide the researchers to design and protect active sites efficiently.
- 3) Electrochemical performance. The rechargeable Zn-air batteries make high claims both on the performance and stability of defective carbon based electrocatalysts. Optimizing synthesis strategies and regulating the doping type, density, location and distribution will still be the focus in the future.
 - 4) Electrochemical measurement. A unified standard should be established to compare the current work as the temperature, atmospheric pressure, mass loading of catalysts and concentration of electrolyte would all affect the electrocatalytic performance. Moreover, Zn plate is generally used as the anode, which is frequently replaced mechanically during the stability test process. Using state-of-the-art zincy anodes could exclude the effect of anodic loss in order to achieve more persuasive results, which could also approach the requirements of application and commercialization.
 - 5) Development of Zn-air batteries. In addition to common aqueous electrolytes, suitable organic electrolytes can also be introduced. And, corresponding oxygen electrocatalysts should be further developed. For practical application, flexible free-standing configuration should be popular. Accordingly, suitable electrocatalysts with high mechanical strength need to be considered, and comprehensive evaluation methods should be developed.

In conclusion, defective carbon-based materials have shown immense potential on oxygen electrodes of rechargeable ZABs. Enormous progress has been made in both defect-designing, characterization and theoretical calculation, while more challenge needs resolving in the future. We hope this review would provide helpful insights and inspire more advanced work in ZABs area.

Acknowledgements

This work is financially supported by NSFC (U1532112, 11574280, 21706248), Innovative Research Groups of NSFC (11621063), CAS Interdisciplinary Innovation Team and CAS Key Research Program of Frontier Sciences (QYZDB-SSW-SLH018), Innovative Program of Development Foundation of Hefei Center for Physical Science and Technology (2016FXCX003). We thank the USTC Center for Micro and Nanoscale Research and Fabrication for kind supports.

Conflict of Interest

The authors declare no conflict of interest.

Keywords: bifunctional catalysis • defective carbon • electrocatalysis • oxygen electrode • rechargeable Zn-air batteries

- [1] a) Z. W. Seh, J. Kibsgaard, C. F. Dickens, I. Chorkendorff, J. K. Norskov, T. F. Jaramillo, *Science* **2017**, *355*; b) M. S. Faber, S. Jin, *Energy Environ. Sci.* **2014**, *7*, 3519.
- [2] A. Sumboja, M. Lübke, Y. Wang, T. An, Y. Zong, Z. Liu, *Adv. Energy Mater.* **2017**, *7*, 1700927.
- [3] a) G. Chai, K. Qiu, M. Qiao, M.-M. Titirici, C. Shang, Z. Guo, *Energy Environ. Sci.* **2017**, *10*, 1186–1195; b) L. Xie, F. Qu, Z. Liu, X. Ren, S. Hao, R. Ge, G. Du, A. M. Asiri, X. Sun, L. Chen, *J. Mater. Chem. A* **2017**, *5*, 7806; c) Z. Cai, D. Zhou, M. Wang, S. M. Bak, Y. Wu, Z. Wu, Y. Tian, X. Xiong, Y. Li, W. Liu, *Angew. Chem.* **2018**, *130*, 9536–9540; *Angew. Chem. Int. Ed.* **2018**, *57*, 9392–9396; d) X. Li, P. Cui, W. Zhong, J. Li, X. Wang, Z. Wang, J. Jiang, *Chem. Commun.* **2016**, *52*, 13233.
- [4] a) C. Zhu, H. Li, S. Fu, D. Du, Y. Lin, *Chem. Soc. Rev.* **2016**, *45*, 517; b) Y. Nie, L. Li, Z. Wei, *Chem. Soc. Rev.* **2015**, *44*, 2168; c) R. Kumar, L. Singh, A. W. Zularisam, *Int. J. Hydrogen Energy* **2017**, *42*, 19287–19295.
- [5] a) L. Jiao, G. Wan, R. Zhang, H. Zhou, S. Yu, H. Jiang, *Angew. Chem.* **2018**, *130*, 8661–8665; *Angew. Chem. Int. Ed.* **2018**, *57*, 8525–8529; b) C. Lin, L. Zhang, Z. Zhao, Z. Xia, *Adv. Mater.* **2017**, *29*, 1606635.
- [6] a) Y. Liang, Y. Li, H. Wang, J. Zhou, J. Wang, T. Regier, H. Dai, *Nat. Mater.* **2011**, *10*, 780–786; b) J. Li, S. Li, Y. Tang, M. Han, Z. Dai, J. Bao, Y. Lan, *Chem. Commun.* **2015**, *51*, 2710; c) J. Lee, S. Kim, R. Cao, N. S. Choi, M. Liu, K. Lee, *Adv. Energy Mater.* **2011**, *1*, 34–50.
- [7] a) Y. Li, M. Gong, Y. Liang, J. Feng, J. E. Kim, H. Wang, G. Hong, B. Zhang, H. Dai, *Nat. Commun.* **2013**, *4*, 1805; b) Y. Lee, J. Suntivich, K. J. May, E. E. Perry, Y. S-Horn, *J. Phys. Chem.* **2012**, *3*, 399–404.
- [8] K. Gong, F. Du, Z. Xia, M. Durstock, L. Dai, *Science* **2009**, *760*–764.
- [9] a) S. Yang, X. Feng, X. Wang, K. Mullen, *Angew. Chem.* **2011**, *123*, 5451–5455; *Angew. Chem. Int. Ed.* **2011**, *50*, 5339–5343; b) T. Ma, S. Dai, M. Jaroniec, S. Qiao, *Angew. Chem.* **2014**, *126*, 7409–7413; *Angew. Chem. Int. Ed.* **2014**, *53*, 7281–7285.
- [10] H. Wang, C. Tang, Q. Zhang, *Catal. Today* **2017**, *301*, 25–31.
- [11] a) Y. Li, W. Zhou, H. Wang, L. Xie, Y. Liang, F. Wei, J. C. Idrobo, S. J. Pennycook, H. Dai, *Nat. Nanotechnol.* **2012**, *7*, 394–400; b) P. Zhang, F. Sun, Z. Xiang, Z. Shen, J. Yun, D. Cao, *Energy Environ. Sci.* **2014**, *7*, 442; c) K. Hartl, M. Hanzilikb, M. Arenz, *Energy Environ. Sci.* **2011**, *4*, 234.
- [12] a) J. Liang, R. Zhou, X. Chen, Y. Tang, S. Qiao, *Adv. Mater.* **2014**, *26*, 6074–6079; b) G. Wu, K. L. More, C. M. Johnston, P. Zelenay, *Science* **2011**, *332*, 443–447; c) X. Sun, Y. Zhang, P. Song, J. Pan, L. Zhuang, W. Xu, W. Xing, *ACS Catal.* **2013**, *3*, 1726–1729.
- [13] a) DOI: 10.1039/c8ee03276a; b) Y. Jia, J. Chen, X. Yao, *Mater. Chem. Front.* **2018**, *2*, 1250–1268; c) C. Tang, H. Wang, X. Chen, B. Li, T. Hou, B. Zhang, Q. Zhang, M. M. Titirici, F. Wei, *Adv. Mater.* **2016**, *28*, 6845–6851.
- [14] Y. Huang, Y. Wang, C. Tang, J. Wang, Q. Zhang, Y. Wang, J. Zhang, *Adv. Mater.* **2018**, 1803800.
- [15] D. Yan, Y. Li, J. Huo, R. Chen, L. Dai, S. Wang, *Adv. Mater.* **2017**, *29*, 1606459.
- [16] a) D. Li, Y. Jia, G. Chang, J. Chen, H. Liu, J. Wang, Y. Hu, Y. Xia, D. Yang, X. Yao, *Chem.* **2018**, *4*, 1–12; b) X. Yan, Y. Jia, X. Yao, *Chem. Soc. Rev.* **2018**, *47*, 7628–7658.
- [17] a) Y. Jiang, L. Yang, T. Sun, J. Zhao, Z. Lyu, O. Zhuo, X. Wang, Q. Wu, J. Ma, Z. Hu, *ACS Catal.* **2015**, *5*, 6707–6712; b) C. Tang, B. Wang, H. Wang, Q. Zhang, *Adv. Mater.* **2017**, *29*; c) S. Jiang, Z. Li, H. Wang, Y. Wang, L. Meng, S. Song, *Nanoscale* **2014**, *6*, 14262–14269; d) Y. Jia, L. Zhang, A. Du, G. Gao, J. Chen, X. Yan, C. L. Brown, X. Yao, *Adv. Mater.* **2016**, *28*, 9532–9538.
- [18] C. Tang, Q. Zhang, *Adv. Mater.* **2017**, *29*.
- [19] a) B. Gong, A. Ikematsu, K. Waki, *Carbon* **2017**, *114*, 526–532; b) G. Zhong, H. Wang, H. Yu, H. Wang, F. Peng, *Electrochim. Acta* **2016**, *190*, 49–56; c) H. S. Oktaviano, K. Yamadab, K. Waki, *J. Mater. Chem.* **2012**, *22*, 25167.
- [20] a) L. Tao, Q. Wang, S. Dou, Z. Ma, J. Huo, S. Wang, L. Dai, *Chem. Commun.* **2016**, *52*, 2764–2767; b) Z. Liu, Z. Zhao, Y. Wang, S. Dou, D. Yan, D. Liu, Z. Xia, S. Wang, *Adv. Mater.* **2017**, *29*.
- [21] D. Deng, L. Yu, X. Pan, S. Wang, X. Chen, P. Hu, L. Sun, X. Bao, *Chem. Commun.* **2011**, *47*, 10016–10018.
- [22] a) Z.-H. Sheng, L. Shao, J.-J. Chen, W.-J. Bao, F.-B. Wang, X.-H. Xia, *ACS Nano* **2011**, *5*, 4350–4358; b) T. Zhou, Y. Zhou, R. Ma, Z. Zhou, G. Liu, Q. Liu, A. Y. Zhu, J. Wang, *Carbon* **2017**, *114*, 177–186; c) N. Wang, B. Lu, L. Li, W. Niu, Z. Tang, X. Kang, S. Chen, *ACS Catal.* **2018**, *8*, 6827–6836; d) S. Chen, J. Bi, Y. Zhao, L. Yang, C. Zhang, Y. Ma, Q. Wu, X. Wang, Z. Hu, *Adv. Mater.* **2012**, *24*, 5593–5597.
- [23] a) Z. Liu, F. Peng, H. Wang, H. Yu, W. Zheng, J. Yang, *Angew. Chem. Int. Ed.* **2011**, *50*, 3257–3261; *Angew. Chem.* **2011**, *123*, 3315–3319; b) D. Yang, D. Bhattacharjya, S. Inamdar, J. Park, J. Yu, *J. Am. Chem. Soc.* **2012**,

- 134, 16127–16130; c) C. Zhang, N. Mahmood, H. Yin, F. Liu, Y. Hou, *Adv. Mater.* **2013**, *25*, 4932–4937.
- [24] a) Z.-H. Sheng, H.-L. Gao, W.-J. Bao, F.-B. Wang, X.-H. Xia, *J. Mater. Chem.* **2012**, *22*, 390; b) L. Yang, S. Jiang, Y. Zhao, L. Zhu, S. Chen, X. Wang, Q. Wu, J. Ma, Y. Ma, Z. Hu, *Angew. Chem. Int. Ed.* **2011**, *50*, 7132–7135; *Angew. Chem.* **2011**, *123*, 7270–7273; c) T. V. Vineesh, M. P. Kumar, C. Takahashi, G. Kalita, S. Alwarappan, D. K. Pattanayak, T. N. Narayanan, *Adv. Energy Mater.* **2015**, *5*, 1500658.
- [25] a) Z. Yang, Z. Yao, G. Li, G. Fang, H. Nie, Z. Liu, X. Zhou, X. Chen, S. Huang, *ACS Nano* **2015**, *6*, 205–211; b) J. E. Park, Y. J. Jang, Y. J. Kim, M. S. Song, S. Yoon, D. H. Kim, S. J. Kim, *Phys. Chem. Chem. Phys.* **2014**, *16*, 103–109.
- [26] C. Zhu, S. Fu, Q. Shi, D. Du, Y. Lin, *Angew. Chem.* **2017**, *129*, 14132–14148; *Angew. Chem. Int. Ed.* **2017**, *56*, 13944–13960.
- [27] M. Ishizaki, S. Akiba, A. Ohtani, Y. Hoshi, K. Ono, M. Matsuba, T. Togashi, K. Kanazuka, M. Sakamoto, A. Takahashi, T. Kawamoto, H. Tanakab, M. Watanabe, M. Arisakac, T. Nankawad, M. Kurihara, *Dalton Trans.* **2013**, *42*, 16049–16055.
- [28] X. Guo, M. Wang, X. Huang, P. Zhao, X. Liu, R. Che, *J. Mater. Chem. A* **2013**, *1*, 8775.
- [29] J. Li, M. Chen, S. Karakatos, Z. Feng, D. A. Cullen, M. Lucero, D. Su, S. Hwang, H. Zhang, K. L. More, G. Wang, C. Lei, M. Wang, H. Xu, B. Li, Z. Wang, G. E. Sterbinsky, G. Wu, K. Liu, *Nat. Catal.* **2018**, 1480959.
- [30] a) S. Mukerjee, S. Srinivasan, M. P. Soriaga, *J. Electrochem. Soc.* **1995**, *142*, 1409–1421; b) Matthew Newville, *J. Synchrotron Radiat.* **2001**, *8*, 322–324; c) C. Roth, N. Martz, T. Buhrmester, J. Scherer, H. Fuessa, *Phys. Chem. Chem. Phys.* **2002**, *4*, 3555–3557.
- [31] C. Yu, X. Han, Z. Liu, C. Zhao, H. Huang, J. Yang, Y. Niu, J. Qiu, *Carbon* **2018**, *126*, 437–442.
- [32] K. Matsubara, K. Waki, *Electrochim. Acta* **2010**, *55*, 9166–9173.
- [33] X. Lu, W. L. Yim, B. H. Suryanto, C. Zhao, *J. Am. Chem. Soc.* **2015**, *137*, 2901–2907.
- [34] K. Waki, R. A. Wong, H. S. Oktaviano, T. Fujio, T. Nagai, K. Kimotob, K. Yamada, *Energy Environ. Sci.* **2014**, *7*, 1950.
- [35] L. Xue, Y. Li, X. Liu, Q. Liu, J. Shang, H. Duan, L. Dai, J. Shui, *Nat. Commun.* **2018**, *9*, 3819.
- [36] K. Suenaga, H. Wakabayashi, M. Koshino, Y. Sato, K. Urita, S. Iijima, *Nat. Nanotechnol.* **2007**, *2*, 358–360.
- [37] a) I.-Y. Jeon, H.-J. Choi, M. Choi, J.-M. Seo, S.-M. Jung, M.-J. Kim, S. Zhang, L. Zhang, Z. Xia, L. Dai, N. Park, J.-B. Baek, *Sci. Rep.* **2013**, *3*, 1810; b) Z. Zhao, M. Li, L. Zhang, L. Dai, Z. Xia, *Adv. Mater.* **2015**, *27*, 6834–6840.
- [38] a) J. Wu, D. Zhang, Y. Wang, B. Hou, *J. Power Sources* **2013**, *227*, 185–190; b) C. V. Rao, Y. Ishikawa, *J. Phys. Chem. B* **2012**, *116*, 4340–4346.
- [39] a) C. Zhang, N. Mahmood, H. Yin, F. Liu, Y. Hou, *Adv. Mater.* **2013**, *25*, 4932–4937; b) Z. Yang, Z. Yao, G. Li, G. Fang, H. Nie, Z. Liu, X. Zhou, X. Chen, S. Huang, *ACS Nano* **2012**, *6*, 205–211.
- [40] H. Yang, J. Miao, S.-F. Hung, J. Chen, H. Tao, X. Wang, L. Zhang, R. Chen, J. Gao, H. Chen, L. Dai, B. Liu, *Sci. Adv.* **2016**, *2*, e1501122.
- [41] X. Li, H. Wang, J. T. Robinson, H. Sanchez, G. Diankov, H. Dai, *J. Am. Chem. Soc.* **2009**, *131*, 15939–15944.
- [42] a) C. H. Choi, H. K. Lim, M. W. Chung, J. C. Park, H. Shin, H. Kim, S. I. Woo, *J. Am. Chem. Soc.* **2014**, *136*, 9070–9077; b) L. Lai, J. R. Potts, D. Zhan, L. Wang, C. K. Poh, C. Tang, H. Gong, Z. Shen, J. Linc, R. S. Ruoff, *Energy Environ. Sci.* **2012**, *5*, 7936.
- [43] a) K. Xie, X. Qin, X. Wang, Y. Wang, H. Tao, Q. Wu, L. Yang, Z. Hu, *Adv. Mater.* **2012**, *24*, 347–352; b) Y. Zhao, R. Nakamura, K. Kamiya, S. Nakanishi, K. Hashimoto, *Nat. Commun.* **2013**, *4*, 2390; c) D. Wei, J. I. Mitchell, C. Tansarawiput, W. Nam, M. Qi, P. D. Ye, X. Xu, *Carbon* **2013**, *53*, 374–379; d) M. Zhou, T. Lin, F. Huang, Y. Zhong, Z. Wang, Y. Tang, H. Bi, D. Wan, J. Lin, *Adv. Funct. Mater.* **2013**, *23*, 2263–2269; e) K. Hernadi, A. Fonseca, J. B. Nagy, D. Bernaerts, A. A. Lucay, *Carbon* **1996**, *34*, 1249–1257.
- [44] J. Zhang, L. Qu, G. Shi, J. Liu, J. Chen, L. Dai, *Angew. Chem.* **2016**, *128*, 2270–2274; *Angew. Chem. Int. Ed.* **2016**, *55*, 2230–2234.
- [45] X. Liu, L. Da, *Nat. Rev. Mater.* **2016**, *1*, 16064.
- [46] T. Wu, C. H. Yeh, W. T. Hsiao, P. Y. Huang, M. Huang, Y. H. Chiang, C. Cheng, R. Liu, P. W. Chiu, *ACS Appl. Mater. Interfaces* **2017**, *9*, 14998–15004.
- [47] J. Wu, C. Jin, Z. Yang, J. Tian, R. Yang, *Carbon* **2015**, *82*, 562–571.
- [48] S. Wang, E. Iyamperumal, A. Roy, Y. Xue, D. Yu, L. Dai, *Angew. Chem. Int. Ed.* **2011**, *50*, 11756–11760.
- [49] J. Liang, Y. Jiao, M. Jaroniec, S. Qiao, *Angew. Chem. Int. Ed.* **2012**, *51*, 11496–11500.
- [50] S. Yang, L. Zhi, K. Tang, X. Feng, J. Maier, K. Müllen, *Adv. Funct. Mater.* **2012**, *22*, 3634–3640.
- [51] M. Borgheia, N. Laocharoena, E. K. Pöldseppb, L.-S. Johansson, J. Campbell, E. Kauppinen, K. Tammeveskib, O. J. Rojas, *Appl. Catal. B*, **2017**, *204*, 394–402.
- [52] Q. Liu, J. Jin, J. Zhang, *ACS Appl. Mater. Interfaces* **2013**, *5*, 5002–5008.
- [53] H. Fei, J. Dong, Y. Feng, C. S. Allen, C. Wan, B. Voloskiy, M. Li, Z. Zhao, Y. Wang, H. Sun, P. An, W. Chen, Z. Guo, C. Lee, D. Chen, I. Shakir, M. Liu, T. Hu, Y. Li, A. I. Kirkland, X. Duan, Y. Huang, *Nat. Catal.* **2018**, *1*, 63–72.
- [54] S. Chen, J. Duan, M. Jaroniec, S. Qiao, *Adv. Mater.* **2014**, *26*, 2925–2930.
- [55] Y. Zhao, L. Yang, S. Chen, X. Wang, Y. Ma, Q. Wu, Y. Jiang, W. Qian, Z. Hu, *J. Am. Chem. Soc.* **2013**, *135*, 1201–1204.
- [56] C. H. Choi, S. H. Park, S. I. Woo, *ACS Nano* **2012**, *6*, 7084–7091.
- [57] a) J. Shao, W. Lv, Q. Guo, C. Zhang, Q. Xu, Q. Yang, F. Kang, *Chem. Commun.* **2012**, *48*, 3706–3708; b) G. A. Ferrero, K. Preuss, A. Marinovic, A. B. Jorge, N. Mansor, D. J. Brett, A. B. Fuertes, M. Sevilla, M. M. Titirici, *ACS Nano* **2016**, *10*, 5922–5932.
- [58] Y. Peng, B. Lu, S. Chen, *Adv. Mater.* **2018**, *30*, 1801995.
- [59] Y. Chen, S. Ji, C. Chen, Q. Peng, D. Wang, Y. Li, *Joule* **2018**, *2*, 1242–1264.
- [60] G. He, X. Han, B. Moss, Z. Weng, S. Gadipellia, F. Lai, A. G. Kafizas, D. J. L. Brett, Z. Guo, H. Wang, I. P. Parkin, *Energy Storage Mater.* **2018**, 2405–8297.
- [61] a) D. Deng, X. Chen, L. Yu, X. Wu, Q. Liu, Y. Liu, H. Yang, H. Tian, Y. Hu, P. Du, R. Si, J. Wang, X. Cui, H. Li, J. Xiao, T. Xu, J. Deng, F. Yang, P. N. Duchesne, P. Zhang, J. Zhou, L. Sun, J. Li, X. Pan, X. Bao, *Sci. Adv.* **2015**, *1*, e1500462; b) P. Yin, T. Yao, Y. Wu, L. Zheng, Y. Lin, W. Liu, H. Ju, J. Zhu, X. Hong, Z. Deng, G. Zhou, S. Wei, Y. Li, *Angew. Chem.* **2016**, *128*, 10958–10963; *Angew. Chem. Int. Ed.* **2016**, *55*, 10800–10805.
- [62] a) S. Zhao, Y. Wang, J. Dong, C.-T. He, H. Yin, P. An, K. Zhao, X. Zhang, C. Gao, L. Zhang, J. Lv, J. Wang, J. Zhang, A. M. Khattak, N. A. Khan, Z. Wei, J. Zhang, S. Liu, H. Zhao, Z. Tang, *Nat. Energy* **2016**, *1*, 16184; b) Y. Wang, L. Tao, Z. Xiao, R. Chen, Z. Jiang, S. Wang, *Adv. Funct. Mater.* **2018**, *28*, 1705356; c) B. Xia, Y. Yan, N. Li, H. Wu, X. Lou, X. Wang, *Nat. Energy* **2016**, *1*, 1–8.
- [63] L. Zhang, J. Fischer, Y. Jia, X. Yan, W. Xu, X. Wang, J. Chen, D. Yang, H. Liu, L. Zhuang, M. Hankel, D. J. Searles, K. Huang, S. Feng, C. L. Brown, X. Yao, *J. Am. Chem. Soc.* **2018**, *140*, 10757–10763.
- [64] a) A. Zitolo, V. Goellner, V. Armel, M.-T. Sougrati, T. Mineva, L. Stievano, E. Fonda, F. Jaouen, *Nat. Mater.* **2015**, *14*, 937–944. b) A. Zitolo, N. Ranjbar-Sahraie, T. Mineva, J. Li, Q. Jia, S. Stamatin, G. F. Harrington, S. M. Lyth, P. Krti, S. Mukerjee, E. Fonda, F. Jaouen, *Nat. Commun.* **2017**, 957, in press.
- [65] K. Jiang, S. Siahrostami, Austin J. Akey, Y. Li, Z. Lu, J. Lattimer, Y. Hu, C. Stokes, M. Gangishetty, G. Chen, Y. Zhou, W. Hill, W.-B. Cai, D. Bell, K. Chan, J. K. Nørskov, Y. Cui, H. Wang, *Chem* **2017**, *3*, 950–960.
- [66] L. Zhang, Y. Jia, G. Gao, X. Yan, N. Chen, J. Chen, M. T. Soo, B. Wood, D. Yang, A. Du, X. Yao, *Chem* **2018**, *4*, 1–13.
- [67] a) J. K. Nørskov, J. Rossmeisl, A. Logadottir, L. Lindqvist, *J. Phys. Chem. B* **2004**, *108*, 17886–17892; b) J. Zhang, Z. Zhao, Z. Xia, L. Dai, *Nat. Nanotechnol.* **2015**, *10*, 444–452.
- [68] A. Holewinski, S. Linic, *J. Electrochem. Soc.* **2012**, *159*, 864–870.
- [69] N. I. Kovtyukhova, Y. Wang, A. Berkdemir, R. C. Silva, M. Terrones, V. H. Crespi, T. E. Mallouk, *Nat. Chem.* **2014**, *6*, 957–963.
- [70] M. Li, L. Zhang, Q. Xua, J. Niu, Z. Xia, *J. Catal.* **2014**, *314*, 66–72.
- [71] B. Lu, T. J. Smart, D. Qin, J. Lu, N. Wang, L. Chen, Y. Peng, Y. Ping, S. Chen, *Chem. Mater.* **2017**, *29*, 5617–5628.
- [72] L. Qu, Y. Liu, J.-B. Baek, L. Dai, *ACS Nano* **2010**, *4*, 1321–1326.
- [73] a) R. A. Sidik, A. B. Anderson, N. P. Subramanian, S. P. Kumaraguru, B. N. Popov, *J. Phys. Chem. B* **2006**, *110*, 1787–1793; b) R. Czerw, M. Terrones, J.-C. Charlier, X. Blase, B. Foley, R. Kamalakaran, N. Grobert, H. Terrones, D. Tekleab, P. M. Ajayan, W. Blau, M. Ruhle, D. L. Carroll, *Nano Lett.* **2001**, *1*, 457–460.
- [74] a) Y. Lin, L. Yang, Y. Zhang, H. Jiang, Z. Xiao, C. Wu, G. Zhang, J. Jiang, Li Song, *Adv. Energy Mater.* **2018**, *8*, 1703623; b) S. Wang, Q. He, C. Wang, H. Jiang, C. Wu, S. Chen, G. Zhang, L. Song, *Small* **2018**, *14*, 1800128.
- [75] L. Osmieri, R. E. Cid, A. H. A. M. Videla, P. Ocón, S. Specchia, *Appl. Catal. B*, **2017**, *201*, 253–265.
- [76] P. Chen, T. Zhou, L. Xing, K. Xu, Y. Tong, H. Xie, L. Zhang, W. Yan, W. Chu, C. Wu, Y. Xie, *Angew. Chem.* **2017**, *129*, 625–629; *Angew. Chem. Int. Ed.* **2017**, *56*, 610–614.
- [77] a) Y. Shao, G. Yin, Z. Wang, Y. Gao, *J. Power Sources* **2007**, *167*, 235–242; b) L. Fu, S. You, G. Zhang, F. Yang, X. Fang, *Chem. Eng. J.* **2010**, *160*, 164–169.
- [78] Y.-J. Wang, B. Fang, D. Zhang, A. Li, D. P. Wilkinson, A. Ignaszak, L. Zhang, J. Zhang, *Electrochim. Energy Rev.* **2018**, *1*, 1–34.

- [79] H. Cheng, M.-L. Li, C.-Y. Su, N. Li, Z.-Q. Liu, *Adv. Funct. Mater.* **2017**, *27*, 1701833.
- [80] X. Liu, M. Park, M. G. Kim, S. Gupta, G. Wu, J. Cho, *Angew. Chem.* **2015**, *127*, 9790–9794; *Angew. Chem. Int. Ed.* **2015**, *54*, 9654–9658.
- [81] S. Dou, L. Tao, J. Huo, S. Wang, L. Dai, *Energy Environ. Sci.* **2016**, *9*, 1320.
- [82] Y. Zhu, C. Guo, Y. Zheng, S. Qiao, *Acc. Chem. Res.* **2017**, *50*, 915–923.
- [83] S. Yang, Q. H. C. Wang, H. Jiang, C. Wu, Y. Zhang, T. Zhou, Y. Zhou, L. Song, *J. Mater. Chem. A* **2018**, *6*, 11281–11287.
- [84] D. Liu, K. Ni, J. Ye, J. Xie, Y. Zhu, L. Song, *Adv. Mater.* **2018**, *1802104*.
- [85] a) A. Alsdairi, J. K. Li, N. Ramaswamy, S. Mukerjee, K. M. Abraham, Q. Y. Jia, *J. Phys. Chem. Lett.* **2017**, *8*, 2881. b) Z. Chen, L. Cai, X. Yang, C. Kronawitter, L. Guo, S. Shen, B. E. Koel, *ACS Catal.* **2018**, *8*, 1238–1247; c) B. L. Kaiser, S. Gul, J. Kern, V. K. Yachandra, J. Yano, *J. Electron Spectrosc. Relat. Phenom.* **2017**, *221*, 18–27; d) H. Jiang, Q. He, X. Li, X. Su, Y. Zhang, S. Chen, S. Zhang, G. Zhang, J. Jiang, Y. Luo, P. M. Ajayan, L. Song, *Adv. Mater.* **2018**, *1805127*; e) X. Li, H.-Y. Wang, H. Yang, W. Cai, S. Liu, B. Liu, *Small Methods*, **2018**, *1700395*.
- [86] a) Q. Jia, N. Ramaswamy, U. Tylus, K. Strickland, J. Li, A. Serov, K. Artyushkova, P. Atanassov, J. Anibal, C. Gumeci, S. C. Barton, M.-T. Sougrati, F. Jaouen, B. Halevi, S. Mukerjee, *Nano Energy*, **2016**, *29*, 65–82; b) Q. Jia, N. Ramaswamy, H. Hafiz, U. Tylus, K. Strickland, G. Wu, B. Barbiellini, A. Bansil, E. F. Holby, P. Zelenay, S. Mukerjee, *ACS nano* **2015**, *9*, 12496–12505; c) J. Masa, W. Xia, M. Muhler, W. Schuhmann, *Angew. Chem. Int. Ed.* **2015**, *54*, 10102–10120; *Angew. Chem.* **2015**, *127*, 10240–10259.
- [87] U. Tylus, Q. Jia, K. Strickland, N. Ramaswamy, A. Serov, P. Atanassov, S. Mukerjee, *J. Phys. Chem. C* **2014**, *118*, 8999–9008.

Manuscript received: January 3, 2019

Revised manuscript received: March 26, 2019

Version of record online: April 10, 2019